ACS APPLIED NANO MATERIALS

www.acsanm.org Article

Correlating the Nanoscale Structural, Magnetic, and Magneto-Transport Properties in $SrRuO_3$-Based Perovskite Thin Films: Implications for Oxide Skyrmion Devices

Gerald Malsch,* Dmytro Ivaneyko,* Peter Milde,* Lena Wysocki, Lin Yang, Paul H. M. van Loosdrecht, Ionela Lindfors-Vrejoiu,* and Lukas M. Eng*

Cite This: *ACS Appl. Nano Mater.* 2020, 3, 1182−1190 Read Online

ACCESS | Metrics & More | Article Recommendations | Supporting Information

ABSTRACT: We investigated the structural and magnetic properties of bare $SrRuO_3$ (SRO) ultrathin films and $SrRuO_3/SrIrO_3/SrZrO_3$ (SRO/SIO/SZO: RIZ) trilayer heterostructures between 10 and 80 K, by comparing macroscopic data using the magneto-optical Kerr effect (MOKE) and magneto-transport (anomalous Hall effect: AHE), with nanoscale fingerprints when applying noncontact scanning force microscopy (nc-SFM) and magnetic force microscopy (MFM). SRO and RIZ ultrathin films were epitaxially grown at 650 °C onto vicinal $SrTiO_3$ (100) single-crystalline substrates to a nominal thickness of 4 and 4/2/2 unit cells (uc), respectively. Our correlated analysis allows associating topographic sample features of overgrown individual layers to their residual magnetization, as is shown here to be relevant for interpreting the macroscopic AHE data. Although the hump-like features in the AHE suggest a magnetically textured skyrmion phase to exist around 55 K associated with the topological Hall effect (THE), both our MOKE and MFM data cannot support this theory for the ultrathin films investigated. In contrast, our SFM/MFM local-scale analysis finds the local coercive field to be strongly dependent on the effective layer thickness and stoichiometry in both the SRO and RIZ samples, with a huge impact on the local band structure. In fact, it is these variations that in turn mimic a potential THE through anomalies in the AHE resistivity loops.

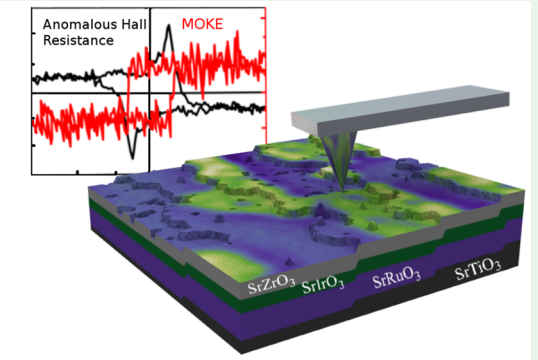

KEYWORDS: *perovskite thin films, skyrmions, topological Hall effect, anomalous Hall effect, magneto-transport properties, magnetic texture*

1. INTRODUCTION

Magneto-transport and Hall measurements are versatile techniques to inspect and characterize magnetically active materials on the micrometer length scale. Extra contributions to the ordinary Hall effect arising through the sample magnetization dependence have been identified as the *anomalous Hall effect* (AHE). In ferromagnetic materials, the AHE usually is proportional to the sample magnetization and therefore shows the same hysteretic behavior.[1,2]

Recently, additional contributions to the AHE have been postulated that arise from topologically nontrivial magnetic textures.[3] This component was labeled as the *topological Hall effect* (THE) and is of great importance when proving the existence of skyrmions by simple transport measurements. As a nontrivial topological magnetic texture, skyrmion lattices (SkLs) are expected to contribute to the THE, being visible as hump-like anomalies on top of the expected AHE.[4] As a conclusion, it is often assumed that any contribution resembling the THE recognized in the Hall data might originate from the presence of skyrmions.[5]

The research field in skyrmion phenomena is given a lot of attention these days, specifically also with the big view of finding the next-generation material that supports skyrmion formation, especially for data storage applications.[6] One avenue of research is to discover an insulating skyrmion host material that would allow electric field manipulation of magnetic domains/phases using standard gating techniques.[7,8] Epitaxial ferromagnetic perovskite oxide heterostructures, offering the possibility to tune the material properties by interfacial engineering, are suitable candidates for skyrmion hosting systems. In the past years, the 4d transition metal $SrRuO_3$ (SRO) attracted much research interest due to the observation of peculiar features appearing in the Hall resistance loops that resembled a THE contribution when SRO was interfaced with the strong SOC $SrIrO_3$ (SIO)[5,8−10] or when it was grown under nonoptimal growth

Received: October 4, 2019
Accepted: January 8, 2020
Published: January 8, 2020

https://dx.doi.org/10.1021/acsanm.9b01918
ACS Appl. Nano Mater. 2020, 3, 1182−1190

conditions.[11,12] These anomalies were attributed either to the formation of skyrmions[5,8,10,13] or to multiple conduction channels of the AHE introduced by off-stoichiometry,[11] disorder,[14] spatial inhomogeneities,[15,16] or interfacial modifications.[17] However, the origin of these anomalies is still under debate since most conclusions are based on the indirect measurement of the transverse Hall resistivity, and the experimental observation of skyrmions by imaging is challenging. In order to elucidate whether the presence of skyrmions causes the THE-like contribution to the Hall resistivity, we combine here magneto-transport with both nanometer- and micrometer-scale spectroscopy/microscopy for inspecting two selected samples, a bare $SrRuO_3$ ultrathin film of a 4uc-thickness (4SRO) and a 4SRO layer overgrown with 2-by-2 unit cells (uc) of $SrIrO_3$ and $SrZrO_3$, resulting in the trilayer 4RIZ heterostructure. Our study unambiguously proves that the origin for the observed THE lies within the 4SRO layer, needing no skyrmions to be present in order to mimic the hump-like features observed in the THE data of the ultrathin films investigated. In turn, the observation of a hump in the AHE is not unique proof for the existence of skyrmions.

2. MATERIAL

$SrRuO_3$ (SRO) constitutes one of the few functional perovskite materials with formula ABO_3 that is ferromagnetic.[18,19] The ferromagnetic order is robust and preserved down to at least 3 unit cells (uc) when epitaxially grown on $SrTiO_3$ (STO) (100) single crystals.[5] Furthermore, SRO films have a large magnetocrystalline anisotropy[20] that is easily manipulated, for instance, through epitaxial heterostructuring. At ordered perovskite interfaces, strong structural coupling via the oxygen octahedra provides a valuable way to engineer magnetic anisotropy, by controlling the easy-axes orientation of the magnetization.[21,22] Magnetic interfacial coupling also provides an appropriate route to manipulate magnetic ordering, for instance, in $SrRuO_3$/$La_{0.7}Sr_{0.3}MnO_3$ superlattices engineered for strong antiferromagnetic interlayer coupling that results in noncollinear magnetic ordering.[23,24]

In 1999, a Lorentz transmission electron microscopy study[25] reported on 30−100 nm thick SRO films reveals magnetic stripe domains that are separated by 3 nm narrow domain walls (DWs). These domains drastically impact the linear magnetoresistance for zero-field-cooled SRO films, as documented by Klein et al.[26] A more recent study reports on a 4 K magnetic force microscopy (MFM) investigation of patterned rectangular magnetic nanoislands of a 10 nm thick SRO film.[27]

With respect to skyrmion formation in heterostructures based on broken inversion symmetry, SRO is a very attractive candidate due to the perpendicular magnetic anisotropy, exhibited when epitaxially grown on single crystalline (sc) STO (100). A very recent example is the work on $SrRuO_3$/$SrIrO_3$ (SRO/SIO) bilayers on STO (100) substrates, in which the ferromagnetic ultrathin SRO layer is interfaced with the paramagnetic SIO that exhibits large spin−orbit coupling (SOC).[5] The inherent inversion symmetry breaking at the interface as well as the proximity of the large SOC of heavy 5d Ir ions are expected to result in a strong interfacial Dzyaloshinskii−Moriya interaction (DMI). The latter may lead to noncollinear magnetic ordering in the ultrathin SRO layers (around 4−6 unit cells) with strong perpendicular magnetic anisotropy.[5,8]

Matsuno et al. showed MFM investigations of a 5 uc-SRO/2 uc-SIO bilayer heterostructure that were claimed to hint toward the formation of tiny bubble-like magnetic domains, interpreted as a possible skyrmion phase.[5] Therefore, we investigate here the magnetic domain formation and morphology in epitaxial ultrathin SRO films and SRO/SIO/SZO (RIZ) heterostructures, in which the SRO layer thickness is kept the same (i.e., 4 uc). We find the nanoscopic origins of SRO layer overgrowth as well as the locally varying coercive field within the 4 uc SRO films to be the origin of macroscopic AHE anomalies, rather than a textured skyrmion phase.

3. SAMPLE PREPARATION

The heterostructures under study [see Figure 1] were fabricated by pulsed-laser deposition (PLD) using a KrF excimer laser.

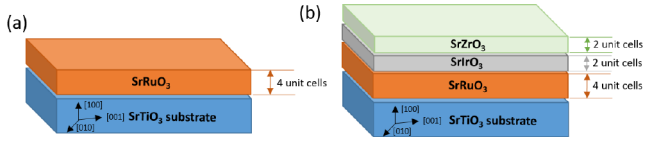

Figure 1. Sample design of (a) the bare SRO thin film with a 4 pseudocubic unit cell thickness (4SRO sample) and (b) the SRO/SIO/SZO trilayer heterostructure made up from 4/2/2 unit cells (4RIZ sample), respectively.

High-oxygen pressure-reflective high-energy electron diffraction (RHEED) was used for both monitoring the layer growth *in situ* and to analyze the film structure at the growth temperature and after cooling (see Section S1 of the Supporting Information). sc-STOs (100) vicinally cut under an angle of about 0.1 °C were used as substrates after etching in buffered HF and annealing at 1000 °C for 2 h in air. These substrates then show a uniform and continuous TiO_2 surface termination, hence providing a stepped sample surface with regularly distributed terraces of 200−450 nm width.

Stoichiometric SRO, SIO, and $SrZrO_3$ (SZO) targets were employed for PLD. The layer growth was performed in a 0.133 mbar O_2 atmosphere, and STO substrates were heated to 650 °C. The laser fluence was set to 2 J/cm^2, while the laser repetition rates for the SRO and SIO/SZO were 5 and 1−2 Hz, respectively. SZO was used here as a protective capping layer on top of the SRO/SIO bilayer, in order to avoid deterioration in the SIO stoichiometry due to moisture.[28] Both the SIO and SZO were grown to a 2 pseudocubic uc thickness each, as determined by RHEED specular spot oscillations. As a result, we obtained a set of 2 samples [see Figure 1]: (a) a 4 uc thin bare SRO sample (furtheron labeled as 4SRO) and (b) a 4/2/2 uc thin SRO/SIO/SZO trilayer heterostructure (labeled furtheron as the 4RIZ sample).

4. MAGNETIC AND MAGNETO-TRANSPORT STUDIES

4SRO and 4RIZ samples first were analyzed at the macroscopic length scale, employing the magneto-optical Kerr effect (MOKE) (for details see Section S2 of the Supporting Information) and magneto-transport measurements using a van der Pauw Hall setup in transverse geometry. In order to suppress the contribution of the linear magnetoresistance, electrical contacts were cyclically permutated to read proper Hall data.

It is commonly assumed that the total Hall resistivity of a ferromagnet is given by the sum of the ordinary Hall resistivity ρ_{OHE} and the anomalous Hall resistivity contribution ρ_{AHE} as

$$\rho_{xy} = \rho_{OHE} + \rho_{AHE} = \mu_0(R_0 H_z + R_A M_z) \quad (1)$$

https://dx.doi.org/10.1021/acsanm.9b01918
ACS Appl. Nano Mater. 2020, 3, 1182−1190

Here, μ_0 is the permeability of a vacuum; R_0 is the Hall coefficient that mainly depends on the majority-charge carrier density; and H_z denotes the magnitude of the external magnetic field applied perpendicular to the *xy*-sample plane. The second term in eq 1 accounts for the anomalous Hall effect exhibited in the presence of a spontaneous magnetization and large spin−orbit coupling; the AHE resistivity is directly proportional to the macroscopic magnetization component M_z perpendicular to the current flow direction,[29] with R_A denoting the anomalous Hall coefficient.[2]

Figure 2 displays the magnetic field dependence of the total Hall resistance as measured for (a) the bare 4SRO thin film and

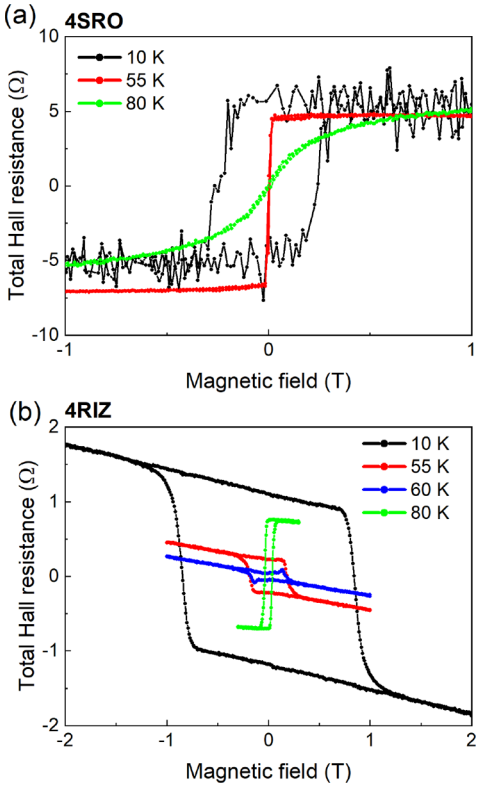

Figure 2. Total Hall resistance loops for (a) the 4SRO film and (b) the 4RIZ trilayer heterostructure. Note that the 4SRO in (a) is paramagnetic above 80 K, while the 4RIZ heterostructure shows an open R_{xy} hysteresis loop proving the ferromagnetic order.

(b) the 4RIZ trilayer heterostructure at selected temperatures. Capping the nominally 4SRO layer with 2-by-2 layers of the strong SOC SIO and the large bandgap insulator SZO results in dramatic changes in both the magnetic and magneto-transport behavior of the SRO layers.

A bare 4SRO thin film exhibits a positive anomalous Hall effect constant R_A within its ferromagnetic phase [Figure 2(a)], while the 4RIZ trilayer shows a negative R_A at low temperatures switching to positive values close to 70 K [Figure 2(b)].

Due to the previously found dependence of the anomalous Hall effect of SRO on the details of its band structure,[30] the observed variations of the AHE characteristics may be related to differences in the crystal structure of the SRO layers.[31] The nonmonotonous AHE temperature dependence already reported for a broad variety of SRO single crystals and epitaxial films[30,31] including our 4RIZ trilayer structure is a clear indication of the structural stabilization of the orthorhombic structure of the SRO layer. Besides playing a protective role against ambient contamination, the capping of the 4 uc SRO layer with the 2 uc SIO/2 uc SZO that has large tilts of the oxygen octahedral is beneficial to stabilize the RuO_6 tilt angles closer to the bulk values of orthorhombic $SrRuO_3$. In contrast, for the sample 4SRO, the structure of the 4 uc SRO grown on the cubic STO substrate and facing vacuum at the top interface is more distorted, and it is likely to be tetragonal with largely suppressed oxygen octahedron tilts down to 10 K. This structural difference may explain why the sample 4RIZ has a larger Curie temperature than the 4SRO sample. The positive sign of the anomalous Hall constant of the 4SRO sample down to 10 K is consistent with a tetragonal structure. The control of the oxygen octahedral structure of ultrathin SRO layers by the deposition of a capping layer has been observed for SRO layers grown on $DyScO_3$ (110) substrates and capped with the cubic STO, where a tetragonal structure was stabilized due to the suppression of the RuO_6 octahedra tilts, with direct impact on the Curie temperature of the ferromagnetic SRO film.[32] In the case of our 4RIZ sample, the enhancement of the ferromagnetic transition temperature of the underlying SRO was observed consistently in our magnetic and magneto-transport investigations.

The Hall resistance loops of the 4SRO films at 80 K exhibit an S-shaped behavior, indicating that the layer must already be in its paramagnetic state.[33] However, at 80 K, the Hall loop of the 4RIZ trilayer still displays an open hysteresis curve, which demonstrates that the SRO layer here is ferromagnetic,[34] in agreement with our MFM investigations (see Section S3.3 for 4SRO and Section S3.5 for 4RIZ of the Supporting Information) and MOKE studies (see Section S2 of the Supporting Information).

In strong magnetic fields where the sample magnetization is assumed to be constant, the total Hall resistance of the bare 4SRO thin film is almost field independent [see Figure 2(a)], whereas the 4RIZ trilayer reveals a negative slope that is attributed to electron-dominated Hall transport [see Figure 2(b)]. This observed difference of the ordinary Hall effect, which determines the total Hall resistance in the high magnetic field range, already indicates severe changes in the electronic band structure for the SRO layer of the 4RIZ trilayer structure, leading to such variations of the charge carrier density in the SRO layers.

Modifications of the electronic band structure have been found to impact the anomalous Hall effect of SRO thin films as well. Due to the dominance of the intrinsic contribution to the AHE,[2,15] determined by the Berry curvature of the conduction bands,[30] the AHE in SRO is sensitive to changes of the band structure. SRO, which exhibits several Weyl nodes in the vicinity of the Fermi level, shows a nontrivial temperature dependence of the AHE, including a sign change from negative to positive close to the Curie temperature, and in the case of orthorhombic single crystals and thin films,[30] it is influenced by the details of the crystal structure,[33] the thickness of the film,[35] the stoichiometry,[11] and the interfacial interactions.[17] For the 4RIZ sample for which the 4 uc SRO layer was capped by SIO/SZO, hump-like anomalies occurred in the Hall resistance loops, close to the temperature where the AHE changes sign (around 55 K), resembling a contribution that could be attributed to the THE. Recently, several works claim the observation of a THE contribution to the AHE resistivity hysteresis loops in SRO ultrathin films[13] and SRO/SIO bilayers.[5,8,12,14] Notably, no such features were detected in our bare 4SRO layers.

https://dx.doi.org/10.1021/acsanm.9b01918
ACS Appl. Nano Mater. 2020, 3, 1182−1190

To clarify such an extra contribution, we compare our AHE with MOKE data obtained *in situ* using a home-built MOKE setup (for details see Section S2 of the Supporting Information). First, when sweeping the external magnetic field, the macroscopic MOKE rotation loops recorded on the 4RIZ thin film resemble the switching behavior of a hard ferromagnetic layer in the easy axis configuration, independent of temperature [see Figure 3]. In fact, MOKE delivers no hints for the existence of an additional nontrivial magnetic phase, as inferred by the Hall measurements. Moreover, the coercive field and the magnetic field of vanishing AHE differ drastically in the temperature range where anomalies in the AHE were observed [see Figure 3(b)].

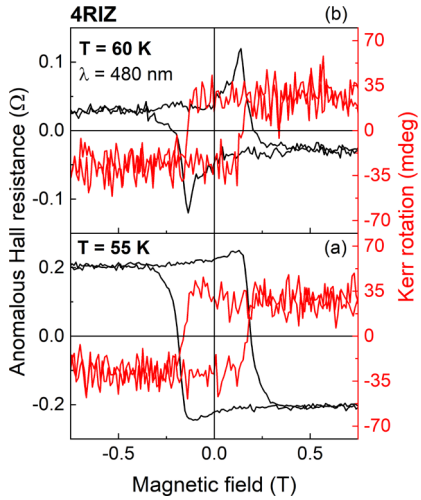

Figure 3. Magnetic field dependence of the anomalous Hall resistance (black) and the Kerr rotation angle (red) for the 4RIZ trilayer sample measured close to the AHE compensation temperature at 55 K (a) and 60 K (b), respectively. MOKE measurements were carried out with incoherent light at λ = 480 nm in order to suppress optical artifacts in these measurements.

These strong discrepancies hence can be solved only with a proper analysis of domain nucleation in SRO thin films and shedding light on those nanoscale processes that unambiguously contribute to magnetization reversal in the 4RIZ heterostructures. We therefore apply low-temperature (LT) noncontact scanning-force microscopy (nc-SFM) and magnetic-force microscopy (MFM) to correlate the macroscopic AHE findings with local-scale structural and magnetic information on both the 4SRO and the 4RIZ samples, respectively. SFM/MFM was performed over the full temperature range from 10 to 80 K; the 55 K results are discussed within the main text here, while all other data can be found in the Supporting Information (see Section S3).

5. LOW-TEMPERATURE SFM AND MFM MEASUREMENTS

The nanoscale analysis of the two sample systems 4SRO and 4RIZ is carried out with our low-temperature (LT) noncontact scanning force microscope (SFM) operating under ultrahigh vacuum (base pressure below 2×10^{-10} mbar). SSS-QMFMR-type MFM probes with a hard magnetic coating were used for both topographic (SFM) and magnetic (MFM) inspection, revealing a mechanical quality factor of $Q \geq 1.45 \times 10^5$. The nominal cantilever oscillation amplitude of 10 nm is kept constant at all times, while then taking the measured frequency shift Δf for topographic and magnetic feedback control in SFM and MFM, respectively.

MFM is performed in a two-path mode, quantifying the sample topography in the first scan while then retracting the tip by 20 nm for the second scan, in order to be sensitive to the longer-range magnetic forces, only.[36]

5.1. Nanoscale Real-Space Analysis of 4SRO and 4RIZ.

Figure 4 displays typical topographic nc-SFM scans of both the 4SRO (a) and the 4RIZ (b) samples. We clearly observe the stepped surface morphology with terraces of a 0.39 nm height extending over 200−450 nm each, as induced by the vicinal STO substrate. Etching the STO substrate prior to the SRO growth for 2.5 min in BHF, it is likely that tiny islands of residual SrO are still present at the STO terrace edges. As discussed by Bachelet et al.,[37] the SRO growth rate is much lower on top of SrO-terminated STO surfaces, leading to trenches in the sample topography marking exactly these positions of the STO terrace edges. Due to the stochastic nature of the deposition process, step edges of the 4SRO surface do not exactly terminate at straight STO step edges, creating areas of sample over- and undergrowth by 5 uc and 3 uc of SRO, respectively. Figure 4(a), (b) shows this behavior for the two samples in a birds-view illustration (*xy*-scan), while Figure 4(c),(d) and Figure 4(e),(f) display the same fact in a cross-sectional and pseudo 3D manner.

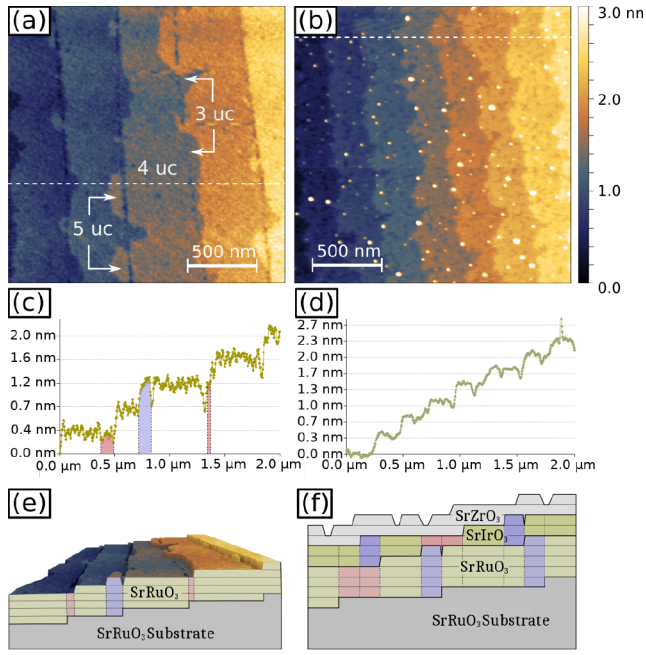

Figure 4. Topographic images of (a) the bare 4SRO film and (b) the 4RIZ trilayer heterostructure. Note the over- and undergrown 5 uc and 3 uc areas in (a). Profiles of the stepped terraces in (c) 4SRO and (d) the 4RIZ heterostructure are taken along the dashed lines in (a) and (b), respectively. (e) Illustration of the differences in layer thickness as caused by under- and overgrowth of 4SRO. (f) Illustration of possible over- and undergrown combinations for the 4RIZ structure.

The 4RIZ structure is presented in Figure 4(b). This topographic scan shows a considerably more disturbed surface arrangement, with both several nanometer high peaks and many dips in the stepped surface, reaching depths comparable to the observed step height. Unlike for the bare 4SRO film, the discrimination of different layer heights is no longer possible since SRO, SIO, and SZO layers intermix in numerous stacking variants, as illustrated in Figure 4(f).

https://dx.doi.org/10.1021/acsanm.9b01918
ACS Appl. Nano Mater. 2020, 3, 1182−1190

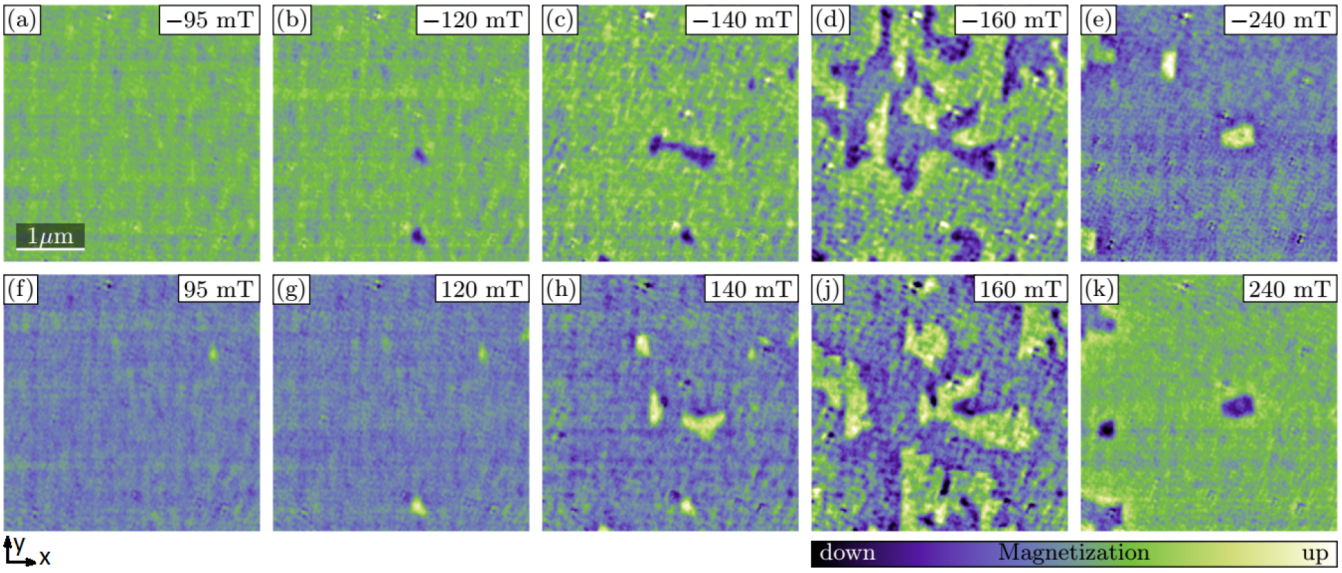

Figure 5. MFM measurements of the 4RIZ trilayer heterostructure at 55 K, showing the domain formation during a forward [(a)−(e), upper row] and reversed magnetic field sweep [(f)−(k), lower row], respectively. Note that all magnetic features laterally extend over many terraces, reaching sizes of micrometers. The full loop of the magnetization reversal of the 4RIZ trilayer heterostructure at 55 K is available as a Web Enhanced Object in the HTML version of the paper.

Step-and-terrace morphology that is typical to films grown in the PLD step-flow growth regime on vicinal substrates turns out to play a crucial role in crystallographic domain formation and growth.[38,39] Preferential alignment with terrace step edges oriented along the [001] orthorhombic axes has been reported for thinner SRO films, while rotation of the magnetic easy axis into the substrate plane is observed for medium-range film thicknesses (between 3 and 7.5 nm).[40] Both our 4SRO and 4RIZ films clearly belong to the first class and scenario, concluding that the easy axis of the 4 uc SRO layer always stands perpendicular to the sample surface. This is of great importance also to our MFM data acquisition and interpretation.

5.2. MFM of the 4RIZ Trilayer Heterostructure. MFM/nc-SFM was applied for inspecting both the 4SRO and 4RIZ thin films at all temperatures. The 4SRO data at 10, 55, and 80 K are found in Sections S3.1, S3.2, and S3.3 of the Supporting Information, respectively, while the 4RIZ MFM inspections are posted in Sections S3.4 and S3.5 of the Supporting Information for 10 and 80 K. The 55 K RIZ findings are discussed now.

A series of relevant MFM images when switching the 4RIZ trilayer heterostructure at 55 K from +2 T to −2 T are illustrated in Figure 5. The terraced substrate sample surface is still vaguely visible, aligned along the *y*-axes in all images. When sweeping from high magnetic fields at +2 T [Figure 5(k)] to the zero-field state, the 4RIZ sample remains fully magnetized, and there are no domains with reversed magnetization formed. This is in full accordance to our hysteresis magnetization loops where the remanent magnetization is equal to the saturated magnetization and consistent with the literature.[41]

Nevertheless, we still observe a low contrast visible along the step edges, due to differences in the magnetic susceptibility of different layer heights that in turn affect the MFM signal strength. At the negative field value of −22 mT, the tip changes its magnetization direction and aligns with the externally applied field.

Domain growth initiates at approximately −100 mT, forming small magnetic nuclei that rapidly increase their domain size when increasing the magnetic field; as shown, the film has mostly switched at −240 mT [see Figure 5(e)], with some isolated areas remaining pinned and stable up to −300 mT.

When reversing the field, we observe strong pinning of both initial magnetic nuclei and the switch-resistant areas, with several sites and domain wall shapes surviving over larger-field changes and field ramping. One also sees that domain growth is affected, but not dominated, by the stepped substrate topography, with sharp vertical domain walls parallel to the terrace direction (*y*-axes) appearing during switching, a clear indication of realignment of the SRO to the topographically induced anisotropy. Nonetheless, as-grown/switched domains extend over multiple terraces, reaching some micrometers in lateral size.

By using Otsu's thresholding method[42] to separate the domains (for details see Section S4 of the Supporting Information), it is possible to extract hysteresis curves from individual MFM images, obtained for both the 4SRO and 4RIZ samples at different temperatures. The temperature dependence of the coercive field is shown in Figure 6 for comparison with MOKE measurements. The width, slope, and coercive fields of MFM hysteresis curves are in good agreement with the hysteresis curves observed by MOKE and therefore are also considerably sharper than the peaks observed in the Hall data. At

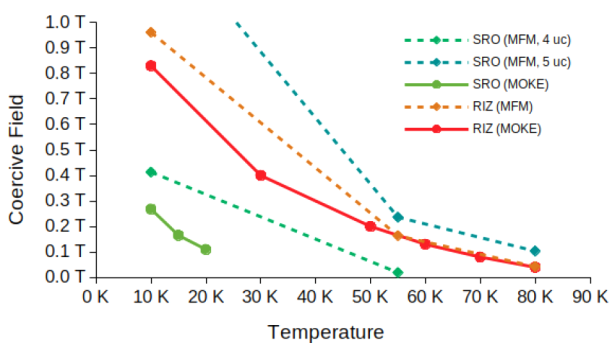

Figure 6. Coercive fields of 4SRO and 4RIZ samples and their areas depending on the number of unit cells.

https://dx.doi.org/10.1021/acsanm.9b01918
ACS Appl. Nano Mater. 2020, 3, 1182−1190

the critical field where the hump-like features start to appear in the AHE, the 4RIZ sample still appears uniformly magnetized under MFM. At no point do we see an intermediate state or second transition indicating the presence of a magnetic structure different from the uniformly polarized domains, skyrmionic or otherwise.

5.3. MFM of Bare 4SRO Thin Films. For comparison reasons, field sweeps of the simpler 4SRO sample were as well investigated by MFM. While full MFM scans at all temperatures of 10, 55, and 80 K are found in Sections S3.1, S3.2, and S3.3 of the Supporting Information, the summarized results for the 10 and 55 K MFM findings on the 4SRO thin films are illustrated in Figure 7.

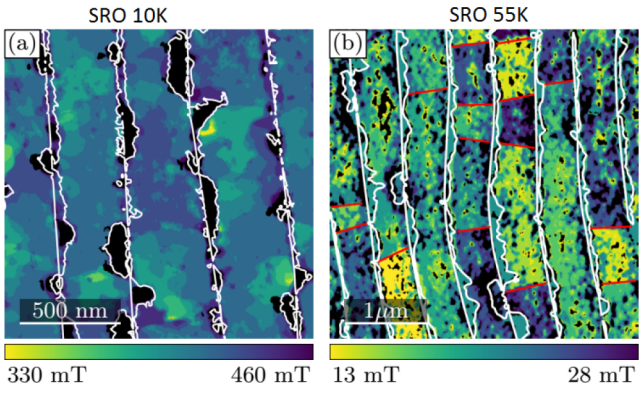

Figure 7. Local switching field of the 4SRO ultrathin film, measured at (a) 10 K and (b) at 55 K. Black areas do not switch within the shown interval. Note the large variation in H_c over the sample areas at nominally the same thickness of 4 uc. This variation is strongly temperature dependent.

What is plotted in Figure 7 is a 2-dimensional map that shows the variation in the average magnetic field value needed to locally switch the sample surface at exactly that sample surface spot. We run a full hysteresis loop at every position of this 512 pixel × 512 pixel image and then deduce (by applying Otsu's method) the corresponding local coercive field.

Notably, provided the thin film sample is homogeneous and defect-free and the growth is independent of any (topographic) structure, the resulting picture should reveal a uniform color/gray shade since all areas/domains must switch at the same coercive field value, independent of temperatures. Concurrently, the error bar would be zero. Nevertheless, what we experimentally observe and display in Figure 7 is that even bare 4SRO is far from being ideal, in that the material switches unevenly: to the one side, the coercive field shows strong variations when plotted over the whole sample area, ranging from 13 to 28 mT at 55 K [Figure 7(b)] with an error bar of 15 mT and 330 to 460 mT at 10 K [Figure 7(a)] with a 130 mT error bar. Rectangular areas along step edges are seen to switch cooperatively as a whole. Note also the black areas in these two figures that correspond to the 5 uc and 3 uc over-/undergrown areas.

Also note from Figure 7 that larger patches displayed in uniform color indicate areas that switch at the same coercive field, as nicely seen for very low temperatures at 10 K [Figure 7(a)]. All the greenish areas in Figure 7 thus are 4 uc SRO layers and hence are expected to show the same switching behavior on the uniformly TiO_2-terminated STO (100) sample surface. Nevertheless, we find these areas to split up into SRO regions that have completely different switching fields, both parallel and perpendicular to the step edges. Variation of the epitaxial strain over the length scale of a terrace width is highly unlikely, which leaves us to conclude that electronic band structure variations for these different patches must be the origin for the documented variable switching behavior.

Also, the underlying anisotropy of the material causes the domains to elongate first perpendicular to the step edges before then growing along them. While at 10 K, this shape asymmetry becomes less pronounced and domain growth is observed both along and perpendicular to the STO step edges [see Figure 7(a)], the material also shows a strong preference for hosting nucleation sites, most preferentially at terrace step edges. This is an indicator that, despite the large difference in coercive fields between the 4SRO and 4RIZ samples, the observed memory effect in the domain growth of the heterostructure is due to these defects within continuous 4SRO layers.

For comparison reasons, the coercive field maps of the 4RIZ structure are displayed as Figure S10 in Section S4 of the Supporting Information, essentially showing similar inhomogeneities like the 4SRO sample.

These field maps can be used for further analysis. We created histograms of areas adjacent to and far from the observed topographic step edges for the 4SRO 10K and 4RIZ 55K measurements to try to correlate changes in the field with these features. The results can be seen in Figure 8: In both cases, the histograms close to the edges are slightly, but not significantly, wider than on the terraces. For SRO, the distribution close to the edges shows a higher number of points switching later, while for RIZ, there is no obvious tendency in either direction. This is not

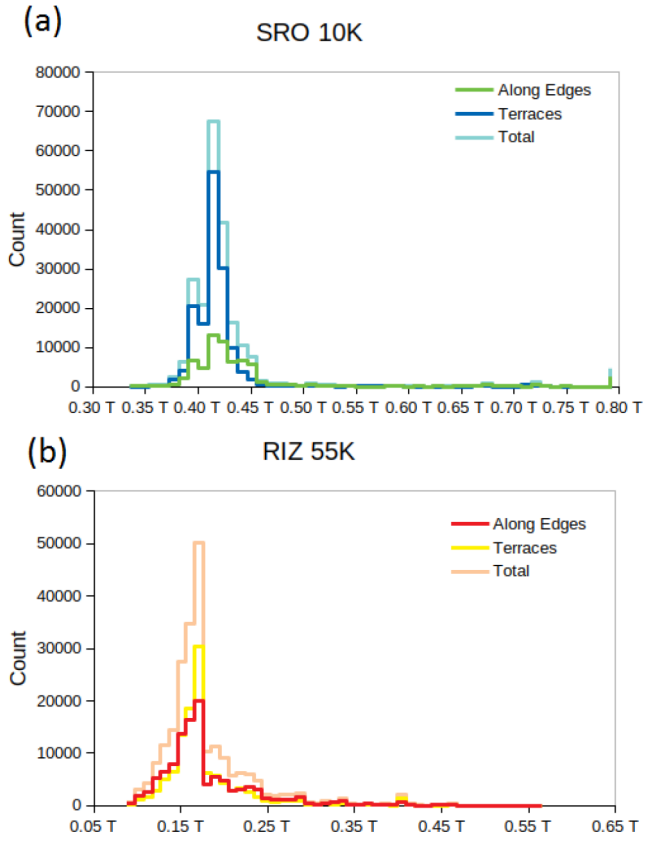

Figure 8. Histograms of the coercive fields per pixel, for the bare 4SRO thin film at 10 K (a) and the 4RIZ trilayer heterostructure at 55 K (b).

https://dx.doi.org/10.1021/acsanm.9b01918
ACS Appl. Nano Mater. 2020, 3, 1182−1190

an artifact of the larger scan range used for the RIZ measurements: If the SRO pictures are downsampled to feature a similar pixel resolution per μm, the resulting histograms retain their shapes and features.

In fact, one might have the impression that domains monitored at an early stage of nucleation or at the later annihilation stage do resemble isolated skyrmion bubbles such as the ones reported for metallic multilayer systems Pt/Co/Ir.[43]

In the literature the number of domains is sometimes correlated with the hump in the AHE.[10,44] In our case, this cannot explain the results for two reasons: First, similar domains are found in both samples at 10 K; however, only the 4RIZ sample shows the THE-like features and this only at temperatures around 55 K, where the AHE resistivity changes sign. Second, the field region where the hump in the AHE is visible is much wider than the field region, where the magnetization reversal takes place. Thus, neither the presence of a number of bubble domains nor the total length of the chiral domain walls can be the origin of the hump-like feature in the AHE.

Speculating about the existence of very tiny—i.e., probably invisible to MFM—skyrmions in the 4RIZ sample at the temperatures and in the field region of the hump-like feature of AHE loops, as suggested in the literature,[5,8] leads to contradicting conclusions. The reason is that the polarity and chirality of skyrmions are generally coupled. Thus, if the magnetization in an area is inverted, necessarily the skyrmions are inverted too, leading to a change of the winding number by twice the number of inverted skyrmions and finally to a sign change of the THE at the coercive field. Alternatively, the skyrmions could be erased under the domain reversal, leading to a vanishing THE signal when the saturated state is reached. Both scenarios can readily be excluded by our combined MOKE/Hall-effect measurements.

Our MFM investigations hence cannot support the presence of any skrymions in these samples, neither isolated skyrmions nor any SkL, as we had found in many other single-crystalline materials.[45−50] What seems much more likely though is that the local sample inhomogeneities (stoichiometry, thickness-variation) reflected through the varying local coercive fields, in the interplay with the SRO−SIO interface (which affects the electronic band structure and thus the AHE sign and magnitude), are the origin for the THE-like behavior in AHE resistivity loops of the 4RIZ heterostructure. The anomalous Hall constant R_A in turn varies slightly and impacts the AHE loops at 55 and 60 K to differ from both the Kerr loops and local-scale magnetization loops acquired by MFM.

6. CONCLUSIONS

Our correlated study involving nc-SFM, MFM, MOKE, and Hall magneto-transport proves that subtle differences in both the structure (RuO_6 octahedral tilts and layer thickness variation) and electronic band structure of the 4 uc SRO-layered thin film are at the origin for anomalies of the Hall loops when the SRO is interfaced with SIO. MOKE and MFM results are extremely consistent when analyzing both types of samples, the bare 4 uc SRO film PLD grown on vicinal STO (100) and the 4SRO overgrown by 2 uc SIO and 2 uc SZO. Our results strongly indicate that anomalies of the Hall resistance loops, which resemble a topological Hall effect contribution, may have other origins than nontrivial topological magnetic domains (e.g., isolated skyrmions or skyrmion lattices). Inhomogeneities of the local thickness may result in variations of the local magnetization switching behavior, reflected in the coercive field strength. In combination with the interfacial modifications at the SRO/SIO interface, which have been shown to impact the sign of the anomalous Hall constant, these inhomogeneities were found to determine the AHE resistivity loop.

■ ASSOCIATED CONTENT

Supporting Information

The Supporting Information is available free of charge at https://pubs.acs.org/doi/10.1021/acsanm.9b01918.

Animation rendering the observation of the magnetization reversal of the bare 4uc SRO thin film at 10 K (MPG)

Animation rendering the observation of the magnetization reversal of the bare 4uc SRO thin film at 55 K (MPG)

Animation rendering the observation of the magnetization reversal of the 4uc RIZ trilayer heterostructure at 10 K (MPG)

Pulsed laser deposition details, MOKE investigations, MFM measurement details on the 4SRO and 4RIZ thin-film samples, and local-scale MFM hysteresis loops and Otsu's method (PDF)

Web-Enhanced Feature

A movie of the full loop of the magnetization reversal of the 4RIZ trilayer heterostructure.

■ AUTHOR INFORMATION

Corresponding Authors

Gerald Malsch − *Institute of Applied Physics, TU Dresden, 01062 Dresden, Germany*; Email: gerald.malsch@tu-dresden.de

Dmytro Ivaneyko − *Institute of Applied Physics, TU Dresden, 01062 Dresden, Germany*; orcid.org/0000-0001-5581-7075; Email: dmytro.ivaneiko@tu-dresden.de

Peter Milde − *Institute of Applied Physics, TU Dresden, 01062 Dresden, Germany*; orcid.org/0000-0002-6844-0905; Email: peter.milde@tu-dresden.de

Ionela Lindfors-Vrejoiu − *II. Physikalisches Institut, Universität zu Köln, 50937 Köln, Germany*; orcid.org/0000-0003-3196-7313; Email: vrejoiu@ph2.uni-koeln.de

Lukas M. Eng − *Institute of Applied Physics and ct.qmat, Dresden-Würzburg Cluster of Excellence - EXC 2147, TU Dresden, 01062 Dresden, Germany*; Email: lukas.eng@tu-dresden.de

Authors

Lena Wysocki − *II. Physikalisches Institut, Universität zu Köln, 50937 Köln, Germany*

Lin Yang − *II. Physikalisches Institut, Universität zu Köln, 50937 Köln, Germany*

Paul H. M. van Loosdrecht − *II. Physikalisches Institut, Universität zu Köln, 50937 Köln, Germany*

Complete contact information is available at: https://pubs.acs.org/10.1021/acsanm.9b01918

Notes

The authors declare no competing financial interest.

■ ACKNOWLEDGMENTS

We thank Achim Rosch for stimulating discussions, for insightful suggestions, and for the calculation of the domain wall length. G.M., D.I., P.M., and L.M.E. gratefully acknowledge financial support by the German Science Foundation (DFG) through the Collaborative Research Center *Correlated Magnetism: From*

Frustration to Topology (CRC1143) project no. 247310070, the SPP2137 (project no. EN 434/40-1), and project no. EN 434/38-1 and no. MI 2004/3-1. L.M.E. also gratefully acknowledges financial support through the *Center of Excellence - Complexity and Topology in Quantum Matter* (ct.qmat) - EXC 2147. I.L.-V. thanks the DFG for financial support (project LI3015/3-1, no. 335038432, and project LI3015/5-1, no. 403504808 within SPP 2137) through the CRC1238.

REFERENCES

(1) Karplus, R.; Luttinger, J. M. Hall Effect in Ferromagnetics. *Phys. Rev.* **1954**, *95*, 1154−1160.
(2) Nagaosa, N.; Sinova, J.; Onoda, S.; MacDonald, A. H.; Ong, N. P. Anomalous Hall Effect. *Rev. Mod. Phys.* **2010**, *82*, 1539−1592.
(3) Bruno, P.; Dugaev, V. K.; Taillefumier, M. Topological Hall Effect and Berry Phase in Magnetic Nanostructures. *Phys. Rev. Lett.* **2004**, *93*, 096806.
(4) Neubauer, A.; Pfleiderer, C.; Binz, B.; Rosch, A.; Ritz, R.; Niklowitz, P. G.; Böni, P. Topological Hall Effect in the *A* Phase of MnSi. *Phys. Rev. Lett.* **2009**, *102*, 186602.
(5) Matsuno, J.; Ogawa, N.; Yasuda, K.; Kagawa, F.; Koshibae, W.; Nagaosa, N.; Tokura, Y.; Kawasaki, M. Interface-Driven Topological Hall Effect in $SrRuO_3$-$SrIrO_3$ Bilayer. *Science Advances* **2016**, *2*, 1600304.
(6) Fert, A.; Cros, V.; Sampaio, J. Skyrmions on the Track. *Nat. Nanotechnol.* **2013**, *8*, 152−156.
(7) Mizuno, H.; Yamada, K. T.; Kan, D.; Moriyama, T.; Shimakawa, Y.; Ono, T. Electric-Field-Induced Modulation of the Anomalous Hall Effect in a Heterostructured Itinerant Ferromagnet $SrRuO_3$. *Phys. Rev. B: Condens. Matter Mater. Phys.* **2017**, *96*, 214422.
(8) Ohuchi, Y.; Matsuno, J.; Ogawa, N.; Kozuka, Y.; Uchida, M.; Tokura, Y.; Kawasaki, M. Electric-Field Control of Anomalous and Topological Hall Effects in Oxide Bilayer Thin Films. *Nat. Commun.* **2018**, *9*, 213.
(9) Wang, L.; Feng, Q.; Kim, Y.; Kim, R.; Lee, K.; Hoon; Pollard, S. D.; Shin, Y. J.; Zhou, H.; Peng, W.; Lee, D.; Meng, W.; Yang, H.; Han, J. H.; Kim, M.; Lu, Q.; Noh, T. W. Ferroelectrically Tunable Magnetic Skyrmions in Ultrathin Oxide Heterostructures. *Nat. Mater.* **2018**, *17*, 1087−1094.
(10) Meng, K.-Y.; Ahmed, A. S.; Baćani, M.; Mandru, A.-O.; Zhao, X.; Bagués, N.; Esser, B. D.; Flores, J.; McComb, D. W.; Hug, H. J.; Yang, F. Observation of Nanoscale Skyrmions in $SrIrO_3$/$SrRuO_3$ Bilayers. *Nano Lett.* **2019**, *19*, 3169−3175.
(11) Kan, D.; Shimakawa, Y. Defect-Induced Anomalous Transverse Resistivity in an Itinerant Ferromagnetic Oxide. *Phys. Status Solidi B* **2018**, *255*, 1800175.
(12) Qin, Q.; Liu, L.; Lin, W.; Shu, X.; Xie, Q.; Lim, Z.; Li, C.; He, S.; Chow, G. M.; Chen, J. Emergence of Topological Hall Effect in a $SrRuO_3$ Single Layer. *Adv. Mater.* **2019**, *31*, 1807008.
(13) Sohn, B.; Kim, B.; Park, S. Y.; Choi, H. Y.; Moon, J. Y.; Choi, T.; Choi, Y. J.; Noh, T. W.; Zhou, H.; Chang, S. H.; Han, J. H.; Kim, C. Emergence of Robust 2D Skyrmions in $SrRuO_3$ Ultrathin Film Without the Capping Layer. *arXiv*, **2018**, 1810.01615.
(14) Wu, L.; Wen, F.; Fu, Y.; Wilson, J. H.; Liu, X.; Zhang, Y.; Vasiukov, D. M.; Kareev, M. S.; Pixley, J. H.; Chakhalian, J. Berry Phase Manipulation in Ultrathin $SrRuO_3$ Films. *arXiv*, **2019**, 1907.07579.
(15) Kan, D.; Moriyama, T.; Kobayashi, K.; Shimakawa, Y. Alternative to the Topological Interpretation of the Transverse Resistivity Anomalies in $SrRuO_3$. *Phys. Rev. B: Condens. Matter Mater. Phys.* **2018**, *98*, 180408.
(16) Wang, L.; Feng, Q.; Lee, H. G.; Ko, E. K.; Lu, Q.; Noh, T. W. Controllable Thickness Inhomogeneity and Berry-Curvature-Engineering of Anomalous Hall Effect in $SrRuO_3$ Ultrathin Films. *arXiv*, **2019**, 1908.08211.
(17) Groenendijk, D. J.; Autieri, C.; van Thiel, T. C.; Brzezicki, W.; Gauquelin, N.; Barone, P.; van den Bos, K. H. W.; van Aert, S.; Verbeeck, J.; Filippetti, A.; Picozzi, S.; Cuoco, M.; Caviglia, A. D. Berry Phase Engineering at Oxide Interfaces. *arXiv*, **2018**, 1810.05619.
(18) Zhu, J.; Li, H.; Zhong, L.; Xiao, P.; Xu, X.; Yang, X.; Zhao, Z.; Li, J. Perovskite Oxides: Preparation, Characterizations, and Applications in Heterogeneous Catalysis. *ACS Catal.* **2014**, *4*, 2917−2940.
(19) Kundu, A. K. *Magnetic Perovskites - Synthesis, Structure and Physical Properties*; Springer, 2016; pp 1−159.
(20) Snyder, G. J. Critical Behavior and Anisotropy in Single Crystal $SrRuO_3$. *arXiv*, **2019**, 1904.12193.
(21) Kan, D.; Aso, R.; Kurata, H.; Shimakawa, Y. Research Update: Interface-Engineered Oxygen Octahedral Tilts in Perovskite Oxide Heterostructures. *APL Mater.* **2015**, *3*, 062302.
(22) Kan, D.; Aso, R.; Sato, R.; Haruta, M.; Kurata, H.; Shimakawa, Y. Tuning Magnetic Anisotropy by Interfacially Engineering the Oxygen Coordination Environment in a Transition Metal Oxide. *Nat. Mater.* **2016**, *15*, 432−438.
(23) Ziese, M.; Bern, F.; Pippel, E.; Hesse, D.; Vrejoiu, I. Stabilization of Ferromagnetic Order in La.07Sr.03MnO_3-$SrRuO_3$ Superlattices. *Nano Lett.* **2012**, *12*, 4276−4281.
(24) Kim, J.-H.; Vrejoiu, I.; Khaydukov, Y.; Keller, T.; Stahn, J.; Rühm, A.; Satapathy, D. K.; Hinkov, V.; Keimer, B. Competing Interactions at the Interface between Ferromagnetic Oxides revealed by Spin-Polarized Neutron Reflectometry. *Phys. Rev. B: Condens. Matter Mater. Phys.* **2012**, *86*, 180402.
(25) Marshall, A. F.; Klein, L.; Dodge, J. S.; Ahn, C. H.; Reiner, J. W.; Mieville, L.; Antagonazza, L.; Kapitulnik, A.; Geballe, T. H.; Beasley, M. R. Lorentz Transmission Electron Microscope Study of Ferromagnetic Domain Walls in $SrRuO_3$: Statics, Dynamics, and Crystal Structure Correlation. *J. Appl. Phys.* **1999**, *85*, 4131−4140.
(26) Klein, L.; Marshall, A.; Reiner, J.; Ahn, C.; Geballe, T.; Beasley, M.; Kapitulnik, A. Large Magnetoresistance of Single-Crystal Films of Ferromagnetic $SrRuO_3$. *J. Magn. Magn. Mater.* **1998**, *188*, 319−325.
(27) Landau, L.; Reiner, J. W.; Klein, L. Low Temperature Magnetic Force Microscope Study of Magnetization Reversal in Patterned Nanoislands of $SrRuO_3$. *J. Appl. Phys.* **2012**, *111*, 07B901.
(28) Groenendijk, D. J.; Manca, N.; Mattoni, G.; Kootstra, L.; Gariglio, S.; Huang, Y.; van Heumen, E.; Caviglia, A. D. Epitaxial Growth and Thermodynamic Stability of $SrIrO_3$/$SrTiO_3$ Heterostructures. *Appl. Phys. Lett.* **2016**, *109*, 041906.
(29) Pugh, E.; Rostoker, N. Hall Effect in Ferromagnetic Materials. *Rev. Mod. Phys.* **1953**, *25*, 151−157.
(30) Fang, Z.; Nagaosa, N.; Takahashi, K. S.; Asamitsu, A.; Mathieu, R.; Ogasawara, T.; Yamada, H.; Kawasaki, M.; Tokura, Y.; Terakura, K. The Anomalous Hall Effect and Magnetic Monopoles in Momentum Space. *Science* **2003**, *302*, 92−95.
(31) Ziese, M.; Vrejoiu, I. Anomalous and Planar Hall Effect of Orthorhombic and Tetragonal $SrRuO_3$ Layers. *Phys. Rev. B: Condens. Matter Mater. Phys.* **2011**, *84*, 1−8.
(32) Thomas, S.; Kuiper, B.; Hu, J.; Smit, J.; Liao, Z.; Zhong, Z.; Rijnders, G.; Vailionis, A.; Wu, R.; Koster, G.; Xia, J. Localized Control of Curie Temperature in Perovskite Oxide Film by Capping-Layer-Induced Octahedral Distortion. *Phys. Rev. Lett.* **2017**, *119*, 177203.
(33) Bern, F.; Ziese, M.; Dörr, K.; Herklotz, A.; Vrejoiu, I. Hall Effect of Tetragonal and Orthorhombic $SrRuO_3$ Films. *Phys. Status Solidi RRL* **2013**, *7*, 204−206.
(34) Shimizu, S.; Takahashi, K. S.; Kubota, M.; Kawasaki, M.; Tokura, Y.; Iwasa, Y. Gate Tuning of Anomalous Hall Effect in Ferromagnetic Metal $SrRuO_3$. *Appl. Phys. Lett.* **2014**, *105*, 163509.
(35) Haham, N.; Shperber, Y.; Schultz, M.; Naftalis, N.; Shimshoni, E.; Reiner, J. W.; Klein, L. Scaling of the Anomalous Hall Effect in $SrRuO_3$. *Phys. Rev. B: Condens. Matter Mater. Phys.* **2011**, *84*, 174439.
(36) Kazakova, O.; Puttock, R.; Barton, C.; Corte-León, H.; Jaafar, M.; Neu, V.; Asenjo, A. Frontiers of Magnetic Force Microscopy. *J. Appl. Phys.* **2019**, *125*, 060901.
(37) Bachelet, R.; Sánchez, F.; Santiso, J.; Munuera, C.; Ocal, C.; Fontcuberta, J. Self-Assembly of $SrTiO_3$(001) Chemical-Terminations: A Route for Oxide-Nanostructure Fabrication by Selective Growth. *Chem. Mater.* **2009**, *21*, 2494−2498.
(38) Gan, Q.; Rao, R. A.; Eom, C. B.; Wu, L.; Tsui, F. Lattice Distortion and Uniaxial Magnetic Anisotropy in Single Domain Epitaxial (110) Films of $SrRuO_3$. *J. Appl. Phys.* **1999**, *85*, 5297−5299.

https://dx.doi.org/10.1021/acsanm.9b01918
ACS Appl. Nano Mater. 2020, 3, 1182−1190

(39) Ziese, M.; Vrejoiu, I.; Hesse, D. Structural Symmetry and Magnetocrystalline Anisotropy of $SrRuO_3$ Films on $SrTiO_3$. *Phys. Rev. B: Condens. Matter Mater. Phys.* **2010**, *81*, 184418.
(40) Schultz, M.; Reiner, J. W.; Klein, L. The Extraordinary Hall Effect of $SrRuO_3$ in the Ultrathin Limit. *J. Appl. Phys.* **2009**, *105*, 07E906.
(41) Xia, J.; Siemons, W.; Koster, G.; Beasley, M. R.; Kapitulnik, A. Critical Thickness for Itinerant Ferromagnetism in Ultrathin Films of $SrRuO_3$. *Phys. Rev. B: Condens. Matter Mater. Phys.* **2009**, *79*, 140407.
(42) Otsu, N. A Threshold Selection Method from Gray-Level Histograms. *IEEE Transactions on Systems, Man, and Cybernetics* **1979**, *9*, 62−66.
(43) Moreau-Luchaire, C.; Moutafis, C.; Reyren, N.; Sampaio, J.; Vaz, C. A. F.; Van Horne, N.; Bouzehouane, K.; Garcia, K.; Deranlot, C.; Warnicke, P.; Wohlhüter, P.; George, J.-M.; Weigand, M.; Raabe, J.; Cros, V.; Fert, A. Additive Interfacial Chiral Interaction in Multilayers for Stabilization of Small Individual Skyrmions at Room Temperature. *Nat. Nanotechnol.* **2016**, *11*, 444−448.
(44) Vistoli, L.; Wang, W.; Sander, A.; Zhu, Q.; Casals, B.; Cichelero, R.; Barthélémy, A.; Fusil, S.; Herranz, G.; Valencia, S.; Abrudan, R.; Weschke, E.; Nakazawa, K.; Kohno, H.; Santamaria, J.; Wu, W.; Garcia, V.; Bibes, M. Giant Topological Hall Effect in Correlated Oxide Thin Films. *Nat. Phys.* **2019**, *15*, 67−72.
(45) Milde, P.; Koehler, D.; Seidel, J.; Eng, L. M.; Bauer, A.; Chacon, A.; Kindervater, J.; Muehlbauer, S.; Pfleiderer, C.; Buhrandt, S.; Schuette, C.; Rosch, A. Unwinding of a Skyrmion Lattice by Magnetic Monopoles. *Science* **2013**, *340*, 1076−1080.
(46) Kézsmárki, I.; Bordács, S.; Milde, P.; Neuber, E.; Eng, L. M.; White, J. S.; Rønnow, H. M.; Dewhurst, C. D.; Mochizuki, M.; Yanai, K.; Nakamura, H.; Ehlers, D.; Tsurkan, V.; Loidl, A. Néel-Type Skyrmion Lattice with confined Orientation in the Polar Magnetic Semiconductor GaV_4S_8. *Nat. Mater.* **2015**, *14*, 1116−1122.
(47) Milde, P.; Neuber, E.; Bauer, A.; Pfleiderer, C.; Berger, H.; Eng, L. M. Heuristic Description of Magnetoelectricity of Cu_2OSeO_3. *Nano Lett.* **2016**, *16*, 5612−5618.
(48) Zhang, S. L.; Bauer, A.; Burn, D. M.; Milde, P.; Neuber, E.; Eng, L. M.; Berger, H.; Pfleiderer, C.; van der Laan, G.; Hesjedal, T. Multidomain Skyrmion Lattice State in Cu_2OSeO_3. *Nano Lett.* **2016**, *16*, 3285−3291.
(49) Butykai, A.; Bordács, S.; Kézsmárki, I.; Tsurkan, V.; Loidl, A.; Döring, J.; Neuber, E.; Milde, P.; Kehr, S. C.; Eng, L. M. Characteristics of Ferroelectric-Ferroelastic Domains in Néel-Type Skyrmion Host GaV_4S_8. *Sci. Rep.* **2017**, *7*, 44663.
(50) Neuber, E.; Milde, P.; Butykai, A.; Bordacs, S.; Nakamura, H.; Waki, T.; Tabata, Y.; Geirhos, K.; Lunkenheimer, P.; Kérsmárki, I.; Ondrejkovic, P.; Hlinka, J.; Eng, L. M. Architecture of Nanoscale Ferroelectric Domains in $GaMo_4S_8$. *J. Phys.: Condens. Matter* **2018**, *30*, 445402.

NOTE ADDED AFTER ASAP PUBLICATION

This paper was published ASAP on January 23, 2020. Because of a production error, the Supporting Information files that are MPG videos were linked to the incorrect descriptions at the end of the paper. The corrected version was reposted on February 13, 2020.

https://dx.doi.org/10.1021/acsanm.9b01918
ACS Appl. Nano Mater. 2020, 3, 1182−1190